

FLOW FIELD ANALYSIS OF RADIAL AND BACKSWEEP CENTRIFUGAL COMPRESSOR IMPELLERS PART I: FLOW MEASUREMENTS USING A LASER VELOCIMETER

D. Eckardt

Motoren- und Turbinen-Union
München GmbH
Formerly, DFVLR
Institut f. Antriebstechnik
Cologne, West Germany

ABSTRACT

The internal flow in 2 centrifugal impellers with radial and backswept discharge, but for the rest identical design, has been investigated at tip speeds of 300 m/s. A laser velocimeter was applied for a detailed flow analysis, besides conventional flow probing and instantaneous wall pressure recordings. While the inducer flow patterns develop similarly up to a 3D flow separation at the shroud, significant differences arise in the second half of the flow channels. Enhanced jet/wake mixing in the backward-curved region provides a less distorted exit flow. The impeller flow evaluation is completed by a comparative discussion of the secondary flow fields and the distinct loss and slip distributions.

NOMENCLATURE

A	=	area
b	=	meridional channel width
C	=	relative curvature
c	=	absolute velocity
c_p	=	specific heat at constant pressure
f	=	relative fluctuation intensity
L2F	=	laser 2focus velocimeter
\dot{m}	=	mass flow rate
n	=	shaft speed
P	=	stagnation pressure
p	=	static pressure
PR	=	stagnation pressure ratio
PS	=	pressure side
R	=	radius
R	=	gas constant
s	=	entropy
s_m	=	meridional shroud contour length
SS	=	suction side
T	=	stagnation temperature
t, t'	=	blade spacing
u	=	impeller velocity
w	=	relative velocity
x	=	coordinate along meridional shroud contour
x/s_m	=	relative meridional shroud contour
y, y'	=	tangential coordinate beg. at PS
$y/t, y'/t'$	=	relative blade spacing
z	=	impeller blade number
z	=	coordinate normal to the shroud beg. at casing wall
z/b	=	relative meridional channel width
I, II, III		
IIIa, IV, V	=	optical measuring areas
β	=	relative flow angle

β_b	=	blade angle
$\Delta\beta$	=	relative deviation angle
δ	=	pressure correction factor for standard conditions
η_s	=	isentropic efficiency, total-to-total
θ	=	temperature correction factor for standard conditions
μ	=	slip factor
φ	=	flow coefficient

Subscripts

0, 1, 2, 3, 4	=	stations in the stage
∞	=	ideal, blade-congruent flow
c	=	curvature
m	=	meridional component
max	=	maximum
min	=	minimum
op	=	optical, L2F focal plane
r	=	radial
rel	=	relative
S	=	standard condition
s	=	isentropic
T	=	total, see def. of $P_{T, rel}$
u	=	component in tangential direction y

Superscripts

-	=	statistical or area average
-	=	mass average
.	=	flow rate

INTRODUCTION

The high performance goals for small gas turbines demand for increased turbine inlet temperatures, pressure ratios and component efficiencies. The development of more efficient high-pressure-ratio centrifugal compressor stages is the indispensable cornerstone for any promising progress in this field.

Since stress problems have become solvable, the centrifugal compressor with backswept blades at impeller tip has displaced the radial discharge type more and more, due to its inherent potential for increased efficiency and range.

In general, efficiency improvements of approximately 2-3 points are to be expected for backsweep angles of 50 to 60 deg (ref. to negative circumferential direction) at pressure ratios between 3.0 and 7.0. By first principles this effect is related to a more advantageous aerodynamic loading and reduced impeller tip Mach numbers, whereas the improved stability stems from the increasing work input with decreasing mass flow.

Detailed flow investigations within high-speed centrifugal compressor impellers are a necessary precondition to set up a sound, physically relevant framework for theoretical

design optimization and performance prediction. In a former paper [1]¹, the internal flow of an impeller with radially ending blades was analyzed by means of laser velocimetry. The next step in the fundamental research program at DFVLR, Cologne, was a comparative flow study within a similar impeller with backward-curved blades at impeller discharge. The nearly identical test set-up should reveal the influence of backward-curvature on compressor performance and operating range, the loading distribution, differences in the incipient flow separation and wake development as well as secondary flow patterns and slip factor relationships.

These investigations and their interpretation in view of the former results are subject of the first part of the present paper, whereas a comparison of experimental data and potential theory calculations is made in part 2.



Fig.1 Test impellers: a - rotor O ($\beta_{2b}=90$ deg)
b - rotor A ($\beta_{2b}=60$ deg)

TEST IMPELLERS

Both centrifugal impellers with the designations - O - for the original radial discharge type and - A - for the alternative design with backswept blades are represented in Fig. 1. Their meridional blade contours and overall dimensions are given in Fig. 2; a detailed data compilation of impeller geometries is attached as appendix to part 2. Both impellers have identical tip diameters, tip

¹ Numbers in brackets designate References at end of paper.

widths, shroud contours, axial lengths and blade numbers ($z=20$). The elliptic shape (in cylindrical sections) of the blade camber line follows the same construction law.

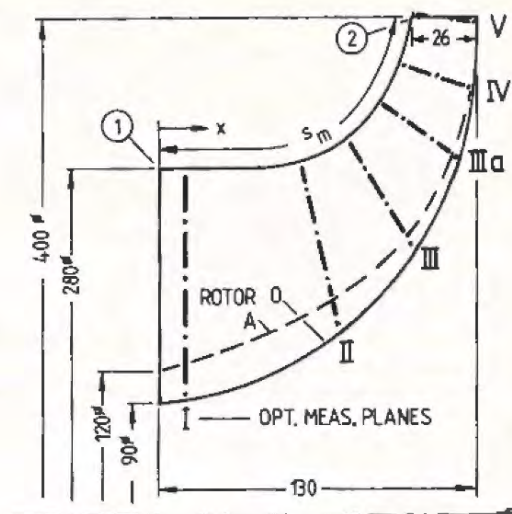


Fig.2 Meridional impeller shapes with L2F measuring planes, dimensions in mm

The backward-curvature of rotor A starts at $R/R_2 = 0.8$ and ends at a blade exit angle of $\beta_{2b} = 60$ deg, referred to the negative circumferential direction, Fig. 3. Rotor A has a reduced inducer inlet area and, correspondingly, a diverging hub profile to match the different volume flow/area relation, especially within the unaltered post-diffuser exhaust ducting.

Certain differences result from the manufacturing techniques. Rotor O, milled out of a block of aluminum alloy, has smooth flow channel surfaces and relatively thin blade leading and trailing edges. On the contrary, rotor A is an aluminum casting with correspondingly rougher surfaces and markedly thicker blades, Fig. 1.

Both impellers were tested in a set-up with vaneless constant-area diffuser up to $R/R_2 = 2$, so that the impeller flow was unaffected by any diffuser distortions. A meridional sketch of the compressor test rig is shown in [1] with the single exception that an axially traversable throttle ring secured axi-symmetric flow conditions at diffuser discharge, instead of the fixed ring in the former set-up. A comprehensive description of the test rig is given in [2].

INSTRUMENTATION

The comparative flow analysis was carried out with 3 stages of instrumentation sophistication:

- conventional, time-mean probe traverses of stagnation pressures and temperatures to determine the overall rotor and stage characteristics,
- instantaneous wall pressure recordings with flush-mounted transducers to analyze the loading distribution along the impeller shroud contour,
- local velocity measurements with the laser 2focus velocimeter (L2F) to reveal the

internal impeller flow patterns.

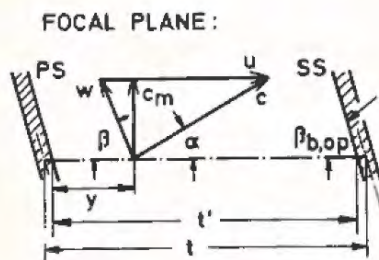
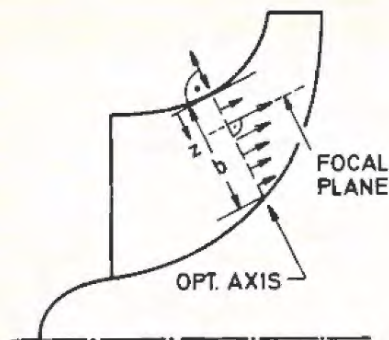


Fig.3 Definition of L2F-measured and calculated velocity components within the impeller flow field

The unsteady pressure distributions were reconstructed by superimposing the correct time-mean pressures, measured with a special (semicircular nozzle) pressure tap [3] and the dynamic transducer recordings. The instantaneous pressures were statistically averaged and digitalized by means of the synchronized sampling technique. This procedure, which avoids errors due to cavity resonance and transducer thermal shift, is described in [2]. The relative error of unsteady pressure measurement is ± 0.5 to 1 per cent.

The L2F technique, developed by Schodl [4], has already been described fundamentally in the context of its first (rotor 0) application [1]. The two-dimensional measuring technique enables direct determination of local absolute velocity vectors (quantity and direction) and their fluctuation intensities in the focal plane, normal to the optical measuring planes, Figs. 2 and 3. Knowing the local circumferential speed, all other components of the velocity triangle can be calculated. Small glass windows, 5 to 20 mm diam, are inserted in the compressor casing, so that measurements are possible in every optically accessible point within the flow channel.

A detailed L2F error analysis, featuring the special aspects of compressor measurements, has already been presented in [1]. In general the statistically mean absolute velocity can be determined with an accuracy of better than ± 1 per cent and the flow angle resolution is to the order of ± 1 deg. Speed and mass flow were computer-controlled and corrected throughout the day-long tests to guarantee reproducible flow conditions.

The impeller flow field was originally analyzed in 5 optical measuring planes I-V, Fig. 2, which were supplemented by plane IIIa for rotor A in the critical area of beginning 3 D flow separation. The relative positions of these L2F measuring planes, aligned normal to the meridional shroud contour, are listed in Table 1.

Table 1 L2F meas. plane positions

Plane No.	x/s_m
I	0.08
II	0.43
III	0.59
IIIa	0.73
IV	0.87
V	1.01

The L2F velocimeter has been further refined since the investigation within rotor 0. Fig. 4 shows the new modular design in which all sub-systems (2-4) around the central unit (1) are exchangeable and adaptable to special measurement demands.

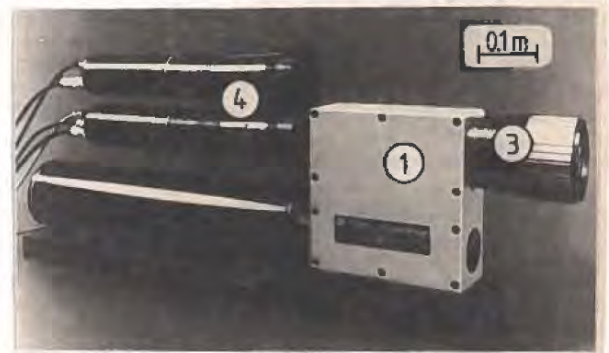


Fig.4 L2F velocimeter (license DFVLR): (1) central unit, (2) laser, (3) image and observation objective, (4) photodetectors

Tip clearances were measured and monitored in both impellers under all running conditions with three capacitive probes, equally spaced along the shroud contour. The effective tip clearance varied, e.g. for $n = 14000 \text{ min}^{-1}$, optimum flow conditions, between 0.5 mm at impeller inlet and exit - and 0.8 mm in the bend to radial.

EXPERIMENTAL RESULTS AND DISCUSSION

Conventional Probe Measurements

Fig. 5 presents the compressor maps of both impellers. The total pressure ratio PR and the isentropic efficiency η_s , total to total, are referenced from the compressor inlet position 0 to the diffuser position 4 at $R/R_2 = 1.667$. Mass flow \dot{m} and speed n are corrected to standard conditions $P_{0g} = 101.33 \text{ kPa}$, $T_{0g} = 288.1^\circ \text{K}$. Stress problems limited the sweptback impeller speed to 16000 min^{-1} .

Both impellers reach the same efficiency levels with slight advantages for rotor 0; the peak efficiencies lie around $\eta_{s,04} = 0.9$, measured within a carefully insulated set-up. Typically the sweptback rotor A has a steeper surge line and a tendency towards an increasing surge margin at higher speeds. But, in

general, the overall impeller tests exhibit no marked differences; a refined experimental analysis is needed to detect deviations between both designs.

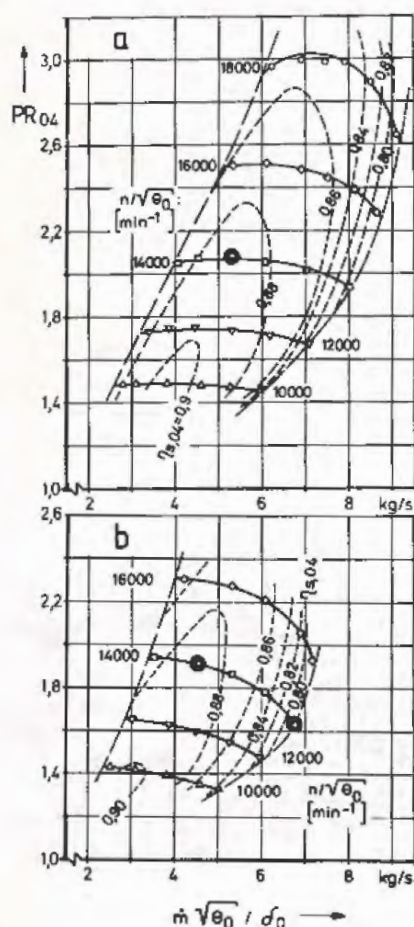


Fig.5 Compressor maps: a - rotor O ($\beta_{2b} = 90^\circ$), b - rotor A ($\beta_{2b} = 60^\circ$), ● - presented L2F data

Three test points on the 14000 min^{-1} speed lines have been selected for detailed discussion, based on L2F data. These points are marked in Fig. 5 and listed in Table 2.

Table 2 Test point characteristics at 14000 min^{-1}

Rotor/Point	$\dot{m} \sqrt{\theta_0} / \delta_0$	PR_{04}	$\eta_{s,04}$
O / Optimum	5.31 kg/s	2.08	.888
A / Optimum	4.54 kg/s	1.91	.886
A / Choke	6.75 kg/s	1.63	.754

Fig. 6 shows the measured stagnation pressure profiles and Fig. 7 compares the corresponding efficiency profiles across the relative diffuser width z/b for both impellers at 14000 min^{-1} , optimum and close to surge and choke flow conditions. The "rotor efficiencies" $\eta_{s,03}$ are based on the stagnation pressure traverses at $R/R_2 = 1.075$ and temperature profiles measured at $R/R_2 = 1.687$ (consequently they include a share of the jet/wake mixing losses in the vaneless diffuser entry region).

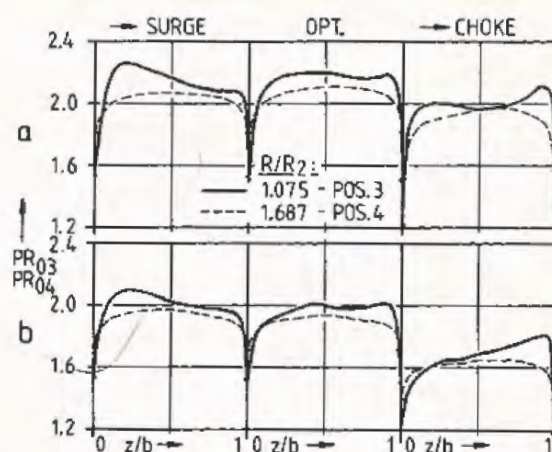


Fig.6 Stagnation pressure profiles at impeller discharge and in the vaneless diffuser, $n = 14000 \text{ min}^{-1}$, a - rotor O, b - rotor A

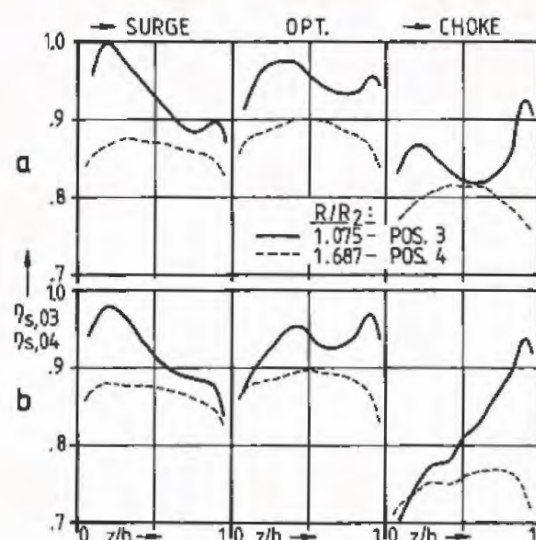


Fig.7 Efficiency profiles at impeller discharge and in the vaneless diffuser, $n = 14000 \text{ min}^{-1}$, a - rotor O, b - rotor A

A few salient features of these distributions are worth mentioning:

- In general, both stages have nearly the same overall efficiencies $\eta_{s,04}$, but the radial discharge impeller shows, at least for optimum and surge flow, higher rotor efficiencies - and correspondingly larger diffuser losses.

- Most striking is the reversing of the efficiency gradient $d\eta_{s,03}/dz$ from diffuser front wall, $z/b = 0$, to the rear wall between choke and surge flow.

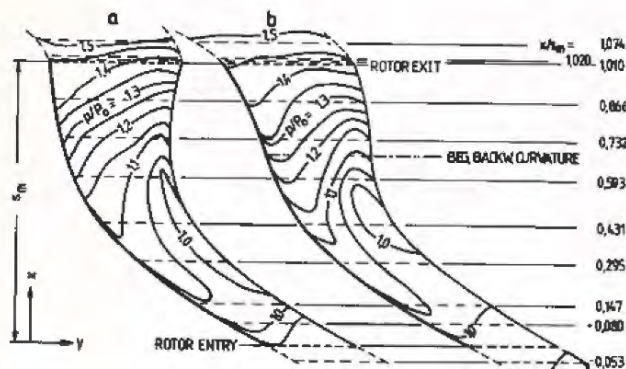
- The surge profiles at impeller discharge exhibit areas of nearly isentropic flow close to the diffuser front wall.

The implications from these observations will be discussed in the context of the laser measurements. A comparison of detailed L2F flow distributions with impeller exit

traverses is also very informative for evaluating the significance of conventional measurements in general.

Unsteady Wall Pressure Recordings

11 water-cooled semiconductor pressure transducers (Kulite XQL-093-25) have been arranged flush-mounted along the shroud from impeller inlet to exit. The resulting pressure distributions for one blade channel at optimum flow conditions are shown in Fig. 8, drawn as isobaric lines of pressure ratio p/p_0 . With respect to the blade channel shape, the left borders correspond to the real x,y-coordinate relations, while the right borders have been found by adding the local blade spacing circumferentially.



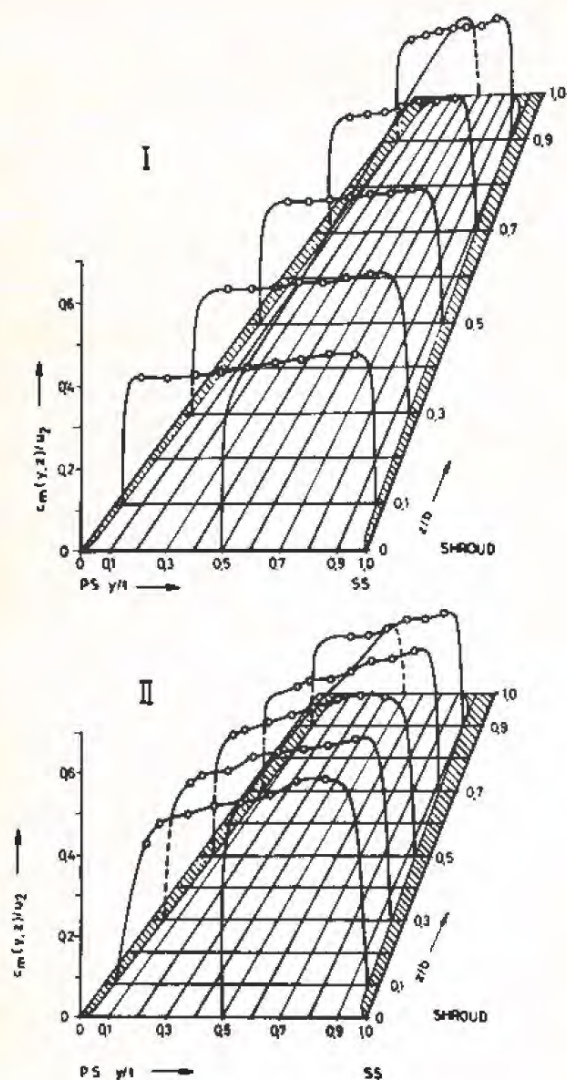


Fig. 9 Rotor A inducer flow, planes I and II, $n = 14000 \text{ min}^{-1}$ optimum

is determined rather from the longer upstream channel shape which is identical to rotor O. This observation is confirmed by considering the corresponding secondary flow and slip distributions, Figs. 16 and 17.

Some of the foregoing observations are understandable in view of the blade curvatures of both impellers, presented in Fig. 13. The influence of channel curvature and rotation on the structure of turbulent shear layers is well-known [5]. E.g., for a usual 90 deg impeller design the stabilizing effects of meridional and blade-to-blade curvature and system rotation superimpose reinforcingly within the bend to radial at the shroud/suction-side corner. One theoretical design measure to encounter the threatening flow separation is to curve the flow channel backwards, thus destabilizing the suction side boundary layer.

Fig. 13 shows the relative curvature distribution of rotors O and A, referring the curvature radius R_C of the 3D blade tip contour to the impeller tip radius R_2 . Sudden curvature

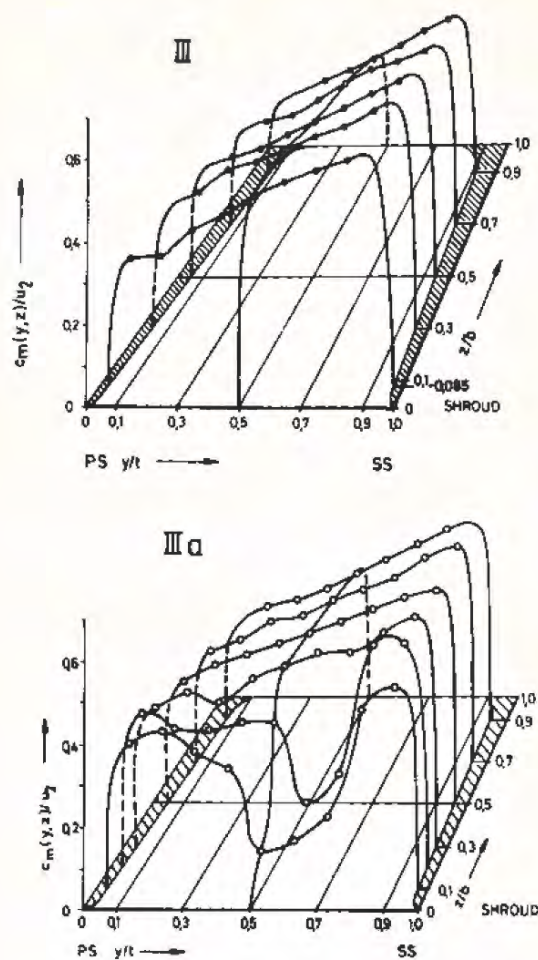


Fig. 10 Rotor A velocity distribution within the bend to radial, planes III and IIIa, $n = 14000 \text{ min}^{-1}$ optimum

changes result from the meridional shroud contour, consisting of circular arcs, and the beginning backsweep.

Actually, first flow distortions occur for both impellers at $x/s_m = 0.6$ - close to the most extreme overall curvature. Obviously the remedy - backward curvature - starts too late, so that it exerts its beneficial effect only on the further wake equalization process of rotor A.

IMPELLER DISCHARGE FLOW AND SLIP EVALUATION

Some additional information, stored in the L2F data, will be analyzed to illustrate the impeller exit flow from various aspects.

Besides the statistically mean absolute velocity \bar{c} , L2F velocimetry also yields the extreme values in the fluctuation spectrum. The relative fluctuation intensity $f = (c_{\max} - c_{\min}) / (2\bar{c})$ characterizes overall flow instabilities, the jet/wake mixing process and the associated loss areas. Fig. 14 compares f -distributions for optimum flow at the exit of both impellers. Noteworthy features are obvious at first glance:

- Excessively high fluctuation intensi-

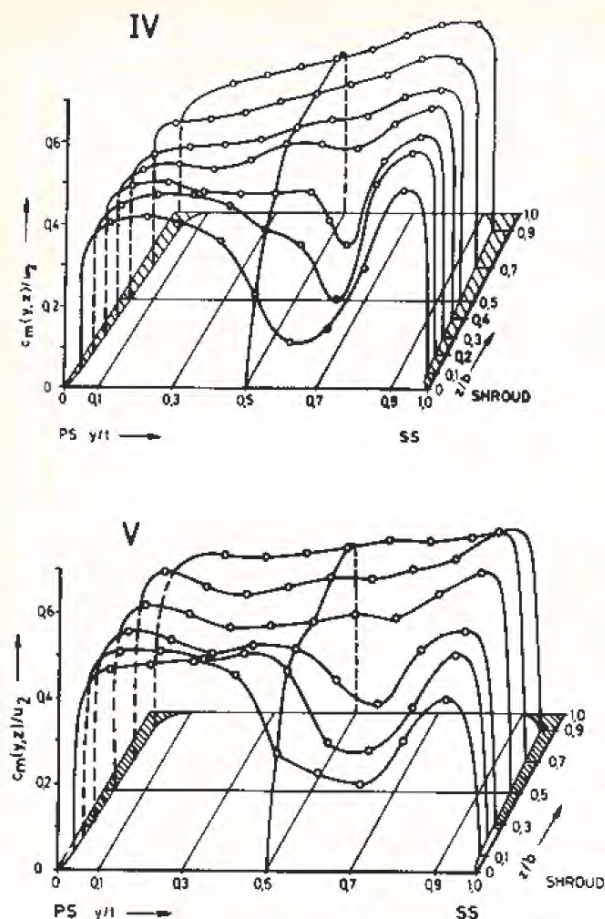


Fig. 11 Rotor A velocity distribution within the backswept exit region, planes IV and V, $n = 14000 \text{ min}^{-1}$ optimum

ties ($f > 0.2$) occur in both cases at nearly the same shroud position ($y/t \approx 0.7$), but less extended for the backswept impeller.

- The differences between high and low fluctuation intensities are less pronounced for rotor A.

- A diagonal separation line limits the area of higher f -values to the shroud/suction side corner of rotor O, while it is spread over the whole shroud stream tube of rotor A.

These differences are closely related to the jet/wake velocity patterns, Figs. 11 and 12b, and the distinct secondary flow behavior of both impellers, Fig. 16.

Another informative picture of the exit flow is revealed by the relative total pressure $P_{T,rel}$, referred to the inlet stagnation pressure at standard conditions $P_{0,s}$. The calculation equation $P_{T,rel}/P_{0,s} = e^{-s/R}$ with s -entropy and R -gas constant has been derived in [1], and more explicitly in [2]. The measurement input consists of instantaneous shroud pressures and L2F-measured absolute velocities in plane V as well as overall temperatures; because of implied simplifications the local uncertainty for the $P_{T,rel}$ -distribution is estimated to be less than ± 2 per cent.

Fig. 15 shows a comparison of rotor A optimum and choke flow; the corresponding rotor O distribution has already been presented in [1].

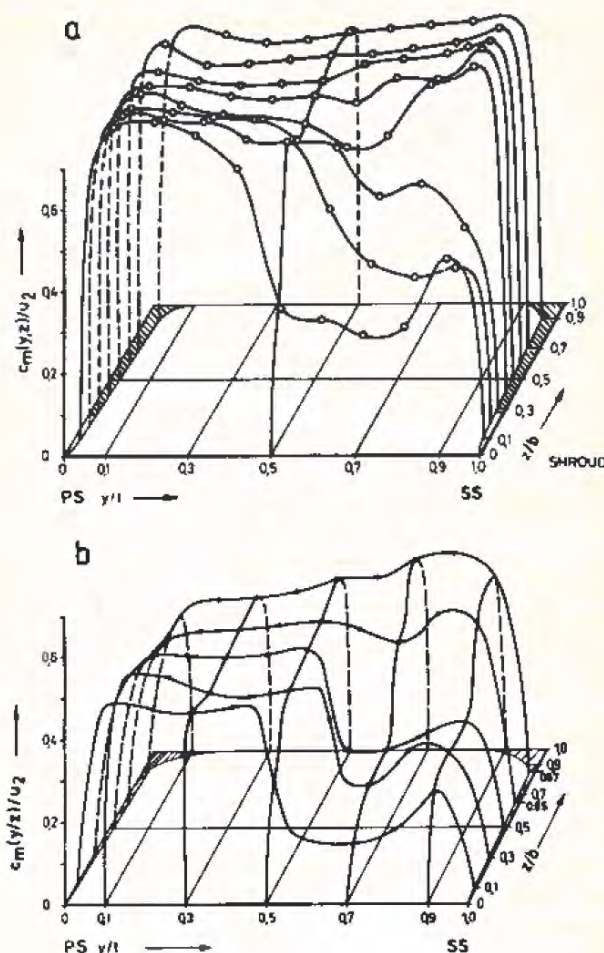


Fig. 12 Velocity distribution at impeller discharge, plane V, $n = 14000 \text{ min}^{-1}$, a - rotor A choke, b - rotor O optimum

By definition the isobars $P_{T,rel}/P_{0,s} = 1.0$ enclose areas of isentropic flow. At first it may be surprising that locally the energy contents are greater than those for one-dimensional, isentropic overall conditions. Similar observations have already been described in early NACA reports [6, 7] and - based on completely different measurement techniques - in [8]. Recently another confirmation of this phenomenon in the low speed range is given - though not commented explicitly - in very thorough measurements by Johnson and Moore [9].

Traupel [10], in a theoretical discussion of the presented $P_{T,rel}$ -distributions, introduced the term "energy classification" (Energieschichtung) for a flow mechanism which should result in a separation of high- and low-energetic fluid particles within the fluctuating relative flow, caused by unsteady Coriolis and inertia forces. Further experimental research on this subject is suggested, preferably in simpler flow configurations (bends, rotating straight diffusers) to gain complementary fundamental data for a realistic centrifugal impeller flow model.

Fig. 15 shows highest losses in the core of the wake area, but far more pronounced for choke flow, while the impression of a more

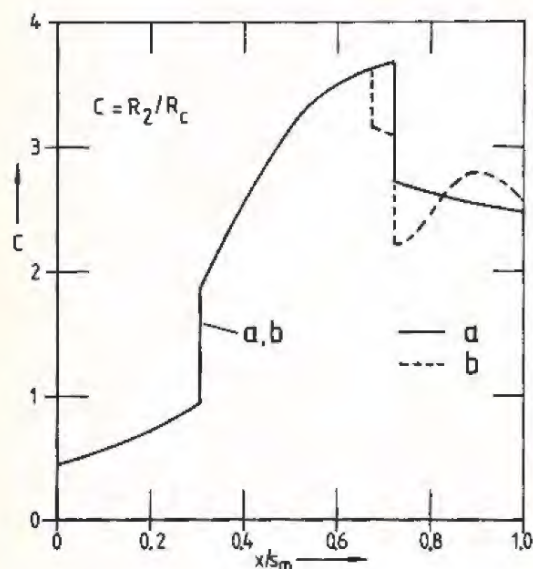


Fig. 13 Spatial blade curvature C along meridional shroud contour x/s_m , a - rotor O ($\beta_{2b} = 90$ deg), b - rotor A ($\beta_{2b} = 60$ deg)

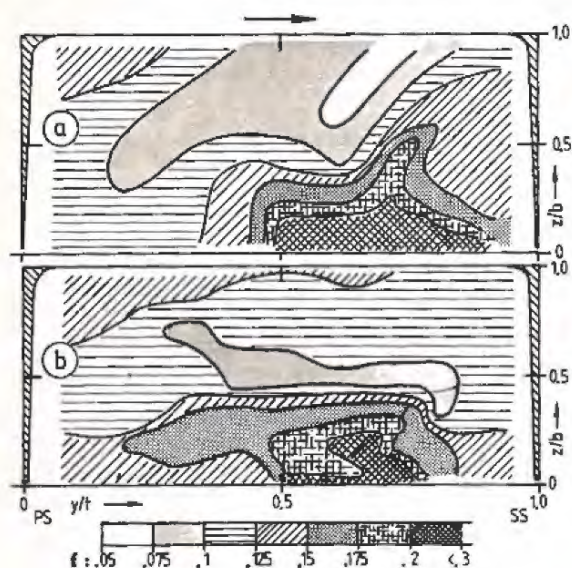


Fig. 14 Relative velocity fluctuation f at impeller discharge, plane V, $n = 14000 \text{ min}^{-1}$ optimum, a - rotor O, b - rotor A

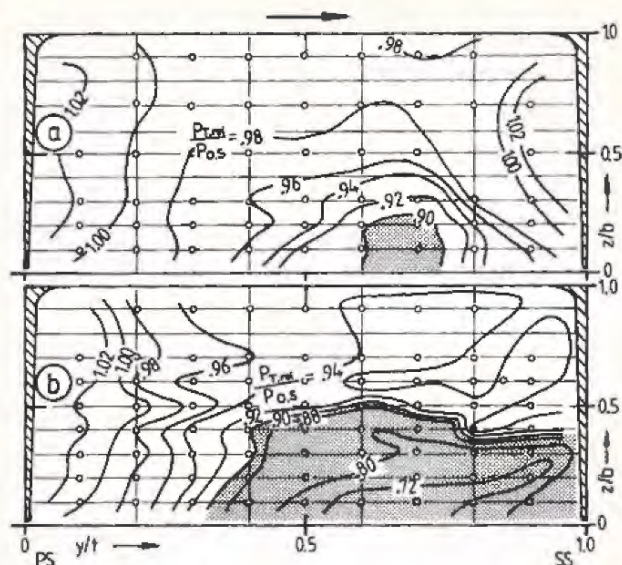


Fig. 15 Relative total pressure distribution at rotor A discharge, plane V, $n = 14000 \text{ min}^{-1}$, a - optimum, b - choke

smoothed-out distribution for optimum flow is confirmed by and large.

With respect to the presented rotor efficiencies of Fig. 7, $R/R_2 = 1.075$, which show slightly lower values for rotor A, optimum, the $P_{T \text{ rel}}$ -distributions in plane V give no definitive answer. Nevertheless an interpretation is suggested that this difference arises not before impeller exit, possibly because of the thicker trailing edges of rotor A. The steep efficiency degradation, Fig. 7, towards the shroud for rotor A, choke flow, is evidently explained by Fig. 15b.

A detailed description of the characteristic secondary flow pattern within centrifugal impellers and its interaction with separation onset and wake development is given in [1], based on L2F measurements in the radial discharge impeller. The principal statements are still valid and need not to be revised for the backswept impeller. The present Fig. 16 concentrates only on exit distributions for the selected operation points of Table 2. As a measure of secondary flow intensities, the plots show distributions of the deviation angle $\Delta\beta = \beta_{b \text{ op}} - \beta$ with $\beta_{b \text{ op}}$ -blade angle and β -relative flow angle in the optical plane V.

Apart from quantitative peculiarities, the following general conclusions can be drawn from Fig. 16:

- The basic secondary flow pattern remains unchanged for the three test cases. Fluid motion in the rear, hub-side part of the channel is counter-balanced by a strong shroud cross flow from pressure to suction side. These phenomena are parts of a dominating main vortex and a weaker clockwise eddy close to the blade suction side, which transport boundary layer material from the hub region towards the shroud.

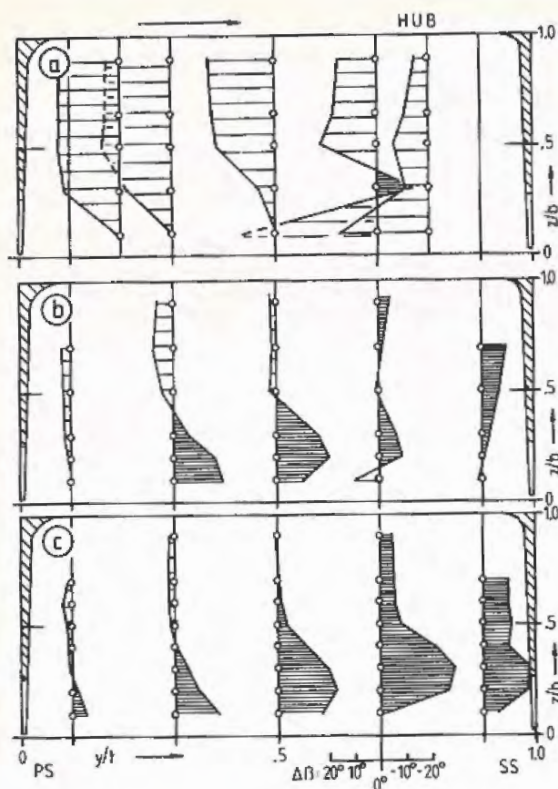


Fig. 16 Distribution of deviation angle $\Delta\beta$, plane V, $n = 14000 \text{ min}^{-1}$, a - rotor O optimum b - rotor A optimum, c - rotor A choke

- The twist of the $\Delta\beta$ -profiles across the blade width for rotor A is perceptibly smaller than for rotor O. Therefore the fluctuation intensity, resulting from the impingement of secondary vortices, and the loss accumulation in the wake area are reduced for the backswep impeller, as has already been observed in Figs. 14b and 15.

- The vortex pattern influences the local energy transfer and consequently the slip distributions in the impellers. This will be discussed in Fig. 17, based on overall data.

This diagram shows the slip factor μ , depending on the flow coefficient φ_2 for both rotors in all compressor operating points (Fig. 5):

$$\mu = \frac{\overline{c_{u2}}}{c_{u2\infty}} = \frac{c_p \Delta T_{04}}{\Delta T_{04} / (u_2^2 (1 - \varphi_2 \cotg \beta_{2b}))} \quad (1)$$

$$\varphi_2 = \frac{\overline{c_{r2}}}{u_2} = \frac{\dot{m}}{A_2 \rho_2 u_2} \quad (2)$$

The μ -determination is based mainly on the measurement of the mass-averaged stagnation temperature rise between stations 0 and 4. The flow coefficient φ_2 is derived by means of the continuity equation at the impeller exit, i.e. the ideal velocity $c_{u2\infty}$ is based on a one-dimensional flow, filling the passage area A_2 completely.

Wiesner's slip relation [11]

$$(\overline{c_{u2\infty}} - \overline{c_{u2}}) / u_2 = \sqrt{\sin \beta_{2b}} / z^{0.7} \quad (3)$$

has been rearranged and plotted accordingly.

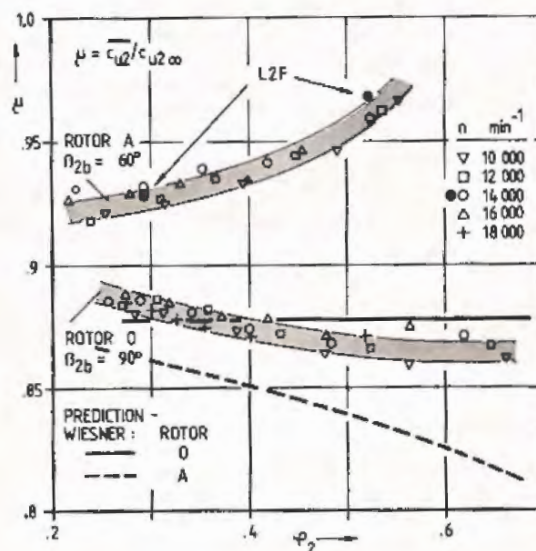


Fig. 17 Variation of slip factor μ with flow coefficient φ_2

The slip factor μ for the radial discharge impeller rises as the flow rate is reduced, i.e. the flow deviates less and less from the blade direction. This corresponds to the usual development for most impeller designs. The coincidence with Wiesner's slip prediction is satisfactory.

On the contrary, rotor A takes a completely different development, resulting in considerable deviations from the predicted curve. Here the slip factor rises with increasing flow, approaching $\mu = 1$ for choke conditions (needless to say that the work input coefficient $\overline{c_{u2}}/u_2$ is still decreasing). This unusual trend has been checked - and confirmed clearly - by mass-integrating the L2F data at rotor A, plane V, for 14000 min^{-1} optimum and choke flow (see Fig. 17, L2F points). A side-effect of this check is, that the share of backflow work in the overall work input is obviously negligible for this test set-up with vaneless diffuser.

The explanation of this phenomenon follows from the S-shaped blade design of impeller A (see Fig. 8b), which turns the flow nearly to the radial direction, until the backswep starts only a short distance from the discharge. The increasing inertia of high flow rates presses the flow in a direction, prescribed by the principal channel curvature, thus ignoring more and more the impeller backswep. The growing flow inclination towards the blade suction side can also be seen in the deviation angle distributions of Figs. 16b, c.

Similar curves have already been predicted theoretically (for separated and attached flows) on an S-shaped, backward-curved impeller with slip factors larger than 1.0 by Sturge and Cumpsty [12].

Summarizing, these results shed light on the intricate and very often contradictory situation of known slip prediction methods for

backswept impellers. In view of the presented results it becomes clear that simple correlations, which refer only to blade number and exit angle, must fail for S-shaped blades with pronounced curvature variations. Accurate work input predictions are decisive for efficient designs of this frequently used centrifugal impeller type. In the future, additional consideration of the impeller blade shape will be mandatory for more reliable slip correlations.

CONCLUSIONS

Two centrifugal impellers which differed mainly in the blade shape at impeller discharge (radially ending and backswept) have been investigated in an identical test set-up with vaneless diffuser.

1 Conventional performance measurements showed no significant differences of both designs. At first glance the high performance level $\eta_{s03} = 0.93$ for optimum conditions does not indicate any advantage of blade backsweep over radial discharge.

2 Detailed comparative L2F measurements revealed clearly that the exit flow distributions of the backward-curved impeller were less distorted. The beneficial effect of blade backsweep on stage efficiency results obviously from a more homogeneous discharge flow at decreased impeller exit Mach numbers, thus improving the vaneless diffuser performance.

3 As for the radial discharge impeller the inducer flow pattern of the backswept impeller corresponds to potential theoretical expectations by and large. This is valid also for the circumferential loading of undistorted areas aft of the beginning wake development.

4 Both impellers show a beginning 3D flow separation at the shroud in the region of greatest tip streamline curvature - with a slight lag for the backswept design. The triggering flow mechanisms are obviously the same, dominated by the identical meridional shroud curvature.

5 The blade backward-curvature begins a short distance downstream; it effects only the wake development. While the pronounced jet/wake pattern increased towards the exit of the radial discharge impeller, the backward-curvature smoothes gradients and levels the extreme differences in velocity and loss distributions. This is caused by destabilizing the shear layers and weakening the secondary flow intensity - resulting in a reduced feeding of low-energetic material into the wake. The principal secondary flow pattern was found to be unchanged for both impellers.

6 The existence of "over-isentropic" areas, i.e. areas in the jet flow at impeller discharge with energy contents larger than those for one-dimensional overall conditions, was shown for both impellers, thus confirming former observations. The basic flow mechanisms (secondary flows, energy classification) were not definitely identified.

7 A comparison of slip factor developments with mass flow showed significant deviations between both rotors. Slip correlations for backswept impellers with marked S-shaped curvature changes must take into account the blade shape as an additional parameter.

ACKNOWLEDGEMENTS

The present measurements were accomplished when the author was with DFVLR, Institut fuer Antriebstechnik, Cologne. This work was supported by a research contract from Forschungsvereinigung Verbrennungskraftmaschinen, a joint research organization of German turbomachinery and combustion engine manufacturers. Promotion of this paper by MTU-Munich is also gratefully acknowledged.

REFERENCES

- 1 Eckardt, D., "Detailed Flow Investigations Within a High-Speed Centrifugal Compressor Impeller," Journal of Fluids Engineering, Trans. ASME, Series I, Vol. 98, 1976, pp. 390-402.
- 2 Eckardt, D., "Investigation of the Jet/Wake Discharge Flow of a Highly Loaded Centrifugal Compressor Impeller," European Space Agency, Techn. Transl. No. 466, 1978, p. 216.
- 3 Weyer, H., "Determination of the Time-Averaged Pressures in Strongly Fluctuating Flows and Especially in Turbo-Machines," RAE library Transl. No. 1850, 1976, p. 150.
- 4 Schodl, R., "Development of the Laser 2 Focus Method for Non-Intrusive Measurement of Flow Vectors, Particularly in Turbomachines," European Space Agency, Techn. Transl. No. 528, 1976, p. 198.
- 5 Johnston, J.P., and Eide, S.A., "Turbulent Boundary Layers on Centrifugal Compressor Blades: Prediction of the Effects of Surface Curvature and Rotation," Journal of Fluids Engineering, Trans. ASME, Series I, Vol. 96, 1976, pp. 374-381.
- 6 Prian, V.D., and Michel, D.J., "An Analysis of Flow in Rotating Passage of Large Radial-Inlet Centrifugal Compressor at Tip Speed of 700 Feet per Second," NASA TN-2584, 1951.
- 7 Hamrick, J.T., Miszisin, J., and Michel, D.J., "Study of Three-Dimensional Internal Flow Distribution Based on Measurements in a 48-Inch Radial-Inlet Centrifugal Impeller," NASA TN-3101, 1954.
- 8 Eckardt, D., "Instantaneous Measurements in the Jet-Wake Discharge Flow of a Centrifugal Compressor Impeller," Journal of Engineering for Power, Trans. ASME, Series A, Vol. 97, 1975, pp. 337-346.
- 9 Johnson, M.W., and Moore, J., "The Development of Wake Flow in a Centrifugal Impeller," ASME Paper No. 79-GT-152, 1979.
- 10 Traupel, W., "Thermische Turbomaschinen," 3rd ed., Vol. 1, Springer Publ., Berlin-Heidelberg-New York, 1977, p. 579.
- 11 Wiesner, F.J., "A Review of Slip Factors for Centrifugal Impellers," Journal of Engineering for Power, Trans. ASME, Series A, Vol. 89, 1967, pp. 558-572.
- 12 Sturge, D.P., and Cumpsty, N.A., "Two-Dimensional Method for Calculating Separated Flow in a Centrifugal Impeller," Journal of Fluids Engineering, Trans. ASME, Series I, Vol. 97, 1975, pp. 581-597.